Fabrication of Magnetic Superstructure $NiFe_2O_4$ @ MOF-74 and Its Derivative for Electrocatalytic Hydrogen Evolution with AC Magnetic Field

Hang-bo Zheng[1], Hui-hui Chen[1], Yuan-li Wang[1], Peng-zhao Gao[1, 2, 3*], Xiao-pan Liu[1,2,3], Evgeny V. Rebrov[4]

[1] College of Materials Science and Engineering, Hunan University, Changsha, Hunan, 410082, China

[2] Hunan Province Key Laboratory for Advanced Carbon Materials and Applied Technology, Hunan University, Changsha, Hunan, 410082, China

[3] Hunan Province Key Laboratory for Spray Deposition Technology and Application, Hunan University, Changsha, Hunan, 410082, China

[4] School of Engineering, University of Warwick, Coventry, CV4 7AL, U. K.

Corresponding author: Peng-zhao Gao

Address: College of Materials Science and Engineering, Hunan University, Changsha, Hunan, 410082, China

Tel: +86 731 88822269; Fax: +86 731 88823554.

Email address: gaopengzhao7602@hnu.edu.cn (Peng-zhao Gao)

Abstract: As an ideal hydrogen production route, electrolyzed water still faces the challenges of high cost of noble-metal electrocatalysts and low performance of non-noble-metal catalysts in scalable applications. Recently, introduction of external fields (such as magnetic fields, light fields, etc.) to improve the electrocatalytic water splitting performance of non-noble-metal catalysts has attracted great attention due to their simplicity. Here, a simple method for preparing magnetic superstructure ($NiFe_2O_4$ @ MOF-74) is described, and the HER behavior of its carbonized derivative, a ferromagnetic superstructure, is revealed in a wide range of applied voltage under an AC magnetic field. The overpotential (@ 10 mA cm^{-2}) required for HER of the ferromagnetic superstructure in 1 M KOH was reduced by 31 mV (7.7 %) when a much small AC magnetic field (only 2.3 mT) is applied. Surprisingly, the promotion effect of the AC magnetic field is not monotonically increasing with the increase of the applied voltage or magnetic field strength, but increasing first, then weakening. This unusual behavior is believed to be mainly caused by the enhanced induced electromotive force and the additional energy by the applied AC magnetic field. This discovery provides a new idea for adjusting the performance of electrocatalytic reactions.

Key words: $NiFe_2O_4$, MOF-74, Magnetic Superstructure, $Fe_{0.64}Ni_{0.36}$, Hydrogen evolution reaction (HER), AC Magnetic field

1 Introduction

The depletion of heavily used fossil fuels as well as its adverse impact on the environment has stimulated continuous efforts to explore novel eco-friendly technologies. Electrocatalytic water splitting is considered a very promising strategy for mitigating the energy crisis and environmental issues[1-2]. Electrocatalytic water splitting is composed of two half reactions of hydrogen evolution reaction (HER) and oxygen evolution reaction (OER) [3-4], and the theoretical minimum decomposition voltage is 1.23 V. However, in practice, an additional potential, namely overpotential, is required to achieve the desired current density due to the slow kinetics[5]. It is a proven strategy to reduce the overpotential via using an electrocatalyst. Noble metal-based electrocatalysts represented by platinum-based, ruthenium-based and iridium-based have demonstrated excellent performance but expensive and scarce in reserves, which have largely limited their commercial applications[6]. Therefore, more and more researchers are focusing on inexpensive transition metal-based electrocatalysts[7-8].

In previous studies, it has been demonstrated that external magnetic fields may affect the electron spin of catalysts and the migration of charge in solution in electrochemical reactions[9-11]. Research by J.A. Koza et al.[12-13] shows that the magnetic fluid convection caused by Lorentz force in the magnetic field can promote the circulation of the electrolyte and accelerate the separation of air bubbles and electrode. Also, the results of KunPeng et al.[14] show that Co_3O_4 / NF exhibits higher OER performance in a DC magnetic field, and it is interpreted as the magnetohydrodynamic effect and the improved spin energy state of the electrons caused by DC magnetic field. Therefore, it is a reasonable and feasible attempt to adjust the performance of magnetic electrocatalyst via external magnetic fields. However, researches on the promotion of electrocatalytic water splitting via magnetic field are

mainly focused on DC magnetic field[15-16]. The effects of AC magnetic field (ACMF) on electrocatalytic water splitting for HER are rarely reported[17]. Also, the intrinsic relationship of ACMF to the activity of HER is unclear.

Hierarchical superstructure with synergistic and enhanced optical, electrical, and magnetic properties have attracted great attention in the fields of catalysis, energy storage, optics, sensing, and drug transportation[18-20] because 3D superstructure constructed from low-dimensional materials can obtain some special advantages while retaining their basic properties[21-22]. To date, many materials such as highly organized building blocks of metals[23], metal-organic frameworks (MOFs) [24] and semiconductors[25-26] have been used to construct 3D superstructure.

In recent years, MOFs have attracted widespread attention in the field of energy as templates[27-29]. Herein, a series of large-curvature ordered magnetic 3D superstructure $NiFe_2O_4$ @ MOF-74 were fabrication by adjusting the content of $NiFe_2O_4$ nanoparticles (NFO NPs) and citric acid. The ferromagnetic 3D superstructure $Fe_{0.64}Ni_{0.36}$ / Fe-Ni-MgO @ C was obtained during subsequent heat treatment, and the pyrolyzed material showed significantly enhanced HER performance. A schematic of the preparation process of 3D superstructure $NiFe_2O_4$ @ MOF-74 and experimental setup are summarized in Scheme 1. In addition, the effect of ACMF on the electrocatalytic activity for HER was investigated with ferromagnetic superstructure as an example. The results showed that the ferromagnetic superstructure all achieves a lower overpotential (@ 10 mA cm^{-2}) under different ACMF, and its magnetic current density increased first and then decreased with the increase of the applied voltage or magnetic field strength. Subsequently, the novel phenomenon was explained in combination with calculations. Here, the magnetic current density is defined as the difference of current density in the presence or absence of an ACMF.

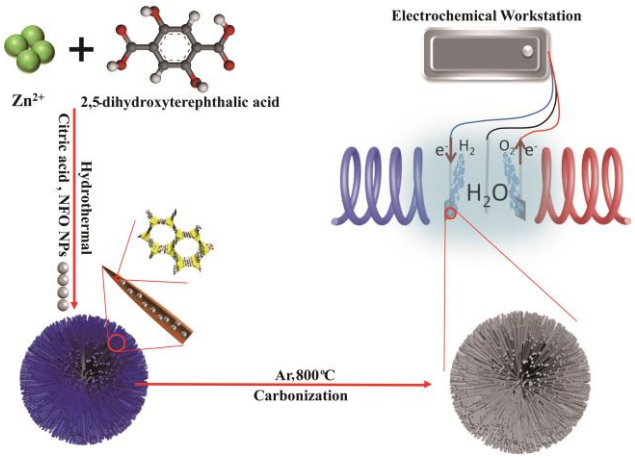

Scheme 1 Illustration of the formation of spherical superstructure of $NiFe_2O_4$ @ MOF-74 and its ferromagnetic derivative for HER with AC magnetic field

2 Results and Discussion

2.1 Fabrication of large-curvature ordered 3D superstructure $NiFe_2O_4$ @ MOF-74

The crystalline structure of samples NM-0, NM-1/8, NM-1/4, and NM-1/2, which represent the composites formed by MOF-74 and 0 g, 0.075 g, 0.15 g, and 0.3g $NiFe_2O_4$, respectively, is analyzed via X-ray diffraction (XRD) as shown in Fig. 1(a). XRD patterns show that 2-theta diffraction peaks located at 6.7, 11.7, 21.7, 25.7, and 31.7° appear in samples NM-0, NM-1/8, NM-1/4, and NM-1/2, which exactly matches the simulated diffraction pattern of reported structure of Mg-MOF-74 (Mg $(H_2O)_2$ $(C_8H_4O_6)$)[30]. However, the intensity of MOF-74 decreases with the increase of NFO NPs content, suggesting worsening crystallinity. In addition, samples NM-1/8, NM-1/4, and NM-1/2 display several new 2-theta diffraction peaks at 30.3, 35.7, and 43.4°, corresponding to the (220), (331), and (400) crystal planes of spinel structure $NiFe_2O_4$ (PDF#54-0964)[31], respectively, which implies the successful synthesis of $NiFe_2O_4$ @ MOF-74 composites. To be more intuitive, TEM images of NFO NPs and sample NM-1/2 are exhibited in Fig. 1(b) and (c), respectively. Some dark particles (3-4 nm in diameter) considered to be NFO NPs are uniformly dispersed in the matrix of sample NM-1/2 and become smaller than original NFO NPs (5-7 nm in diameter), which indicates that NFO NPs has partially dissolved as Eq. 1[32-33].

$$H^+ + NiFe_2O_4 \xrightarrow{\text{Hydrothermal}} Ni^{2+} + Fe^{3+} + H_2O \qquad \text{Eq. 1}$$

The surface compositions and the oxidation states of sample NM-1/2 are further characterized by XPS analysis. And the signals of Mg 1s, Fe 2p, Ni 2p, O 1s, and C 1s are all detected (Fig. 1(d)). As shown in high resolution spectra of Fe 2p and Ni 2p, the presence of Fe ions is confirmed by two peaks at 710.1 and 723.5 eV (Fe $2p_{3/2}$ and $2p_{1/2}$) with an energy difference of 13.4 eV (Supporting Information, Fig. S3(a))[34], presence of Ni ions is confirmed by two peaks at 854.2 and 871.9 eV (Ni $2p_{3/2}$ and $2p_{1/2}$) with an energy difference of 17.7 eV (Supporting Information, Fig. S3(b))[35], repsectively. For more details, peaks at 709.9 and 711.5 eV of Fe $2p_{3/2}$ and 855.3 and 858.0 eV of Ni $2p_{3/2}$ is known as $NiFe_2O_4$ phase (Fig. 1(f-g)) [36-37], and peak at 1303.4 eV of Mg 1s belongs to Mg^{2+} in Mg-MOF-74 (Fig. 1(e)) [30, 38]. Moreover, peaks at 708.6 eV of Fe $2p_{3/2}$ and 853.9 eV of Ni $2p_{3/2}$ could be attributed to coordination of dissolved Fe ions and Ni ions with DHTA[39] as described in Eq. 2, respectively.

$$Mg^{2+} + Ni^{2+} + Fe^{3+} + DHTA \longrightarrow (Mg, Ni, Fe)\text{-}MOF\text{-}74 \qquad \text{Eq. 2}$$

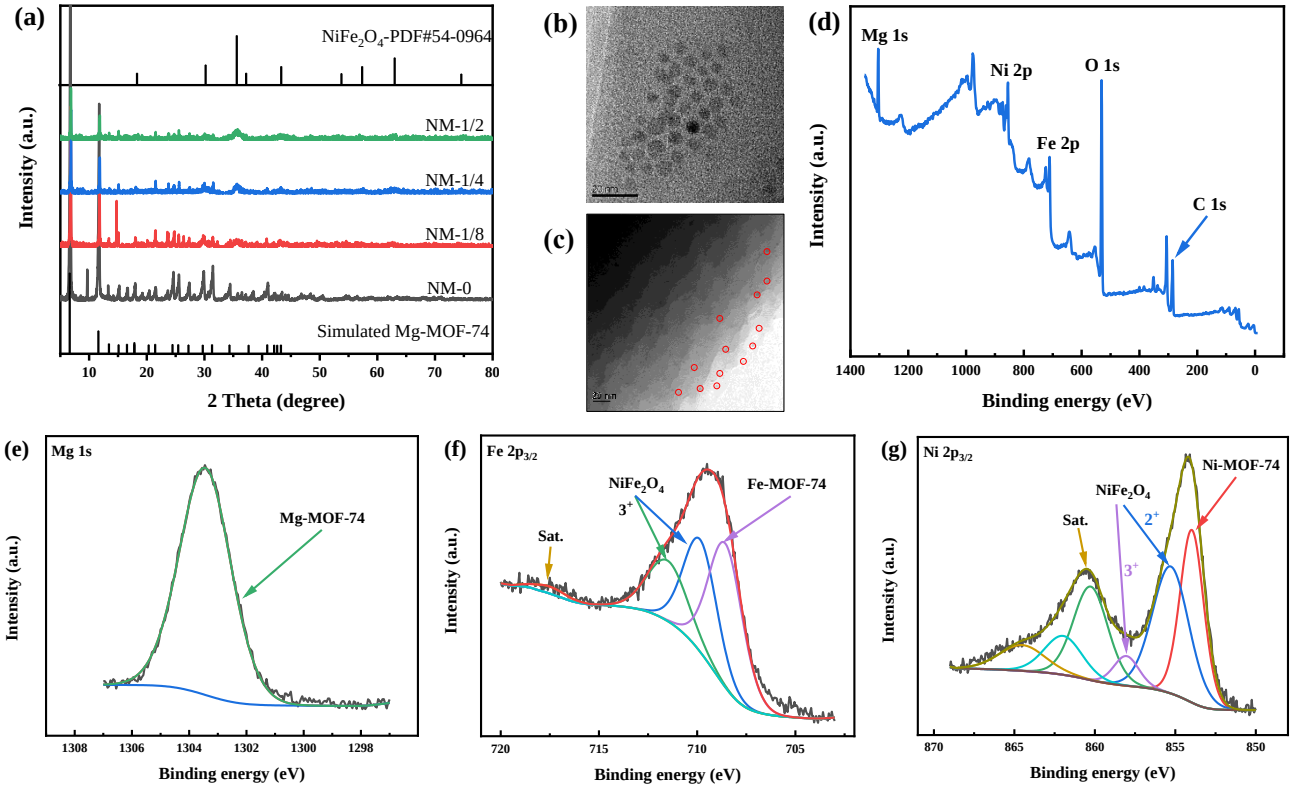

Figure 1 (a) XRD patterns of samples NM-0, NM-1/8, NM-1/4, and NM-1/2; TEM images of NFO NPs (b) and sample NM-1/2 (c); (d) XPS wide spectrum and (e) Mg 1s, high resolution spectra of (f) Fe $2p_{3/2}$, and (g) Ni $2p_{3/2}$ for sample NM-1/2

Fig. 2 exhibits N_2 adsorption / desorption isotherms and pore size distribution curves for samples NM-0, NM-1/8,

NM-1/4, and NM-1/2. As shown in Fig. 2, a rapid increase of N_2 adsorption at lower relative pressure and a noticeable hysteresis loop in a high relative pressure region of 0.4-1.0 are observed in the N_2 sorption isotherms of samples NM-0, NM-1/8, NM-1/4, and NM-1/2, and the pore size distribution of these samples all exhibit two peaks, demonstrating the existence of hierarchical pore structure of those samples[22, 40]. However, samples NM-1/8, NM-1/4, and NM-1/2 shows lower BET surface areas than that of sample NM-0 due to their low crystallinity but larger pore volumes (Table 1) caused by the dissolution of NFO NPs creating additional voids nearby[41-42].

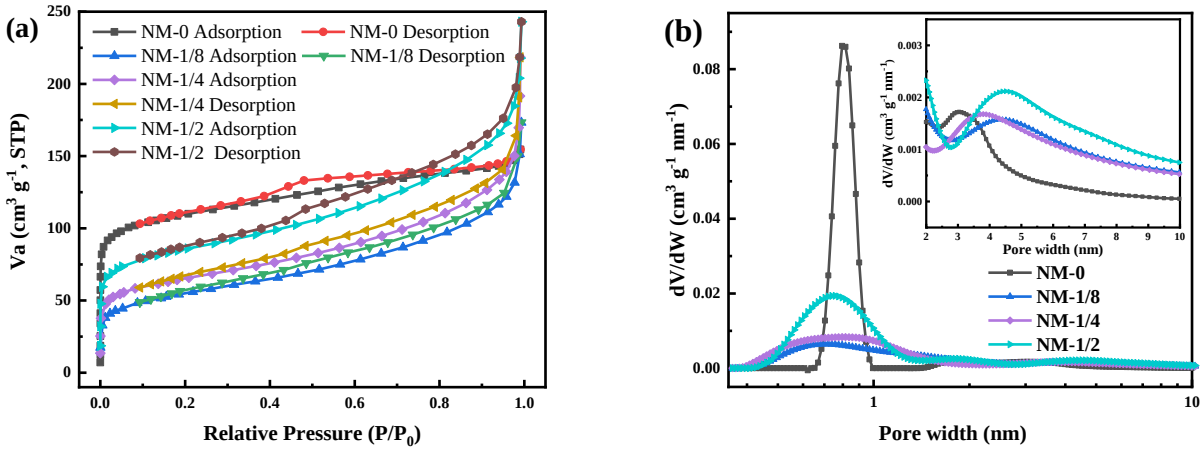

Figure 2 (a) N_2 adsorption / desorption isotherms and (b) pore size distribution of samples NM-0, NM-1/8, NM-1/4, and NM-1/2

Table 1 BET surface areas and pore volumes of samples NM-0, NM-1/8, NM-1/4, and NM-1/2

Sample	NM-0	NM-1/8	NM-1/4	NM-1/2
BET surface areas (m^2 g^{-1})	415.2	202.6	239.2	312.8
pore volumes (cm^3 g^{-1})	0.24	0.27	0.34	0.38

Fig. 3 reveals the effect of NFO NPs on the morphology of MOF-74 via FE-SEM images. Sample NM-0, pure Mg-MOF-74, shows ellipsoidal morphology consisting of prismatic MOF-74 sub-micron rods; while samples NM-1/8, NM-1/4 and NM-1/2 all show novel spherical superstructure with an average diameter of approximately 6 μm, furthermore, samples NM-1/8 and NM-1/4 display a dandelion-like spherical superstructure with a thick and thin prismatic secondary structure, respectively, while sample NM-1/2 exhibits a hollow urchin-like spherical superstructure with a needle-like secondary structure. Series of reference samples were synthesized to demonstrate the formation of this spherical superstructure. Needle-like morphology appears from sample MM-1/4 and samples

MM-1/8 and MM-1/16 also form spherical superstructures (Supporting Information, Fig. S4), indicating that low concentration of dissolved Fe and Ni ions play the key role on the formation of this superstructure. Moreover, the introduction of metal ions via the dissolution of NFO NPs could keep the local concentration of metal ions at a certain concentration, thereby promoting the formation of the uniform superstructures.

Time-dependent experiments of sample NM-1/2 were produced to further understand the formation process of the spherical superstructure (Supporting Information, Fig. S5). It can be seen that at the initial stage, MOF-74 nucleated on the surface of NFO NPs, and then agglomerated into the spherical particles. In the subsequent growth process, the spherical particles formed hollow structure explained by Ostwald ripening theory[43-44]. Especially, samples NM-1/8 and NM-1/4 also possess hollow structures but a smaller aperture (Supporting Information, Fig. S6), caused by a lower NFO NPs content resulting in a reduced amount of heterogeneous nucleation and a lower total surface energy. At the same time, the spherical particles began to split and grow in three dimensions from the surface until a complete 3D superstructure was formed[39, 45-46].

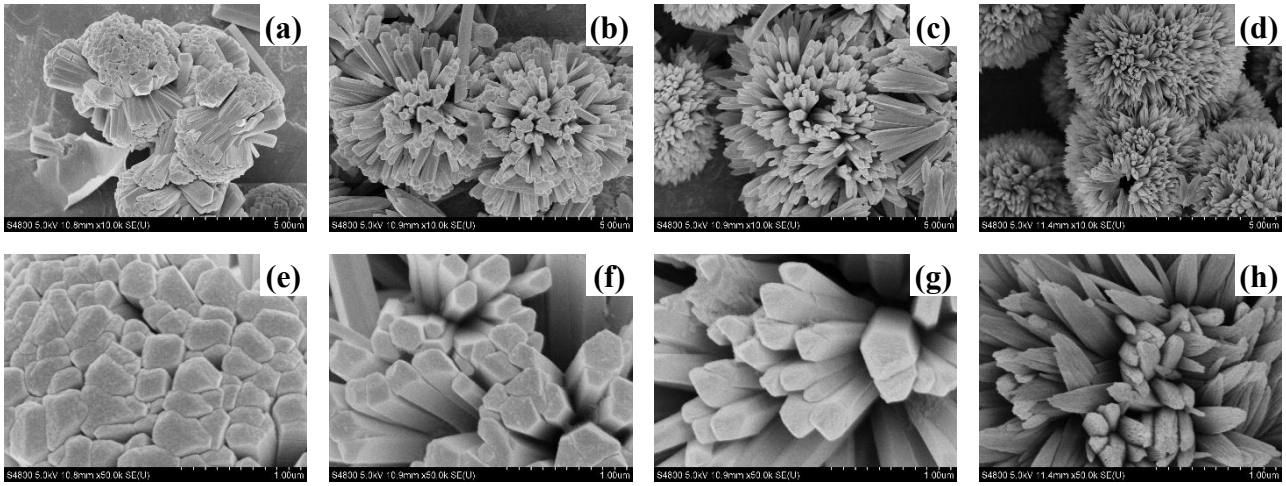

Figure 3 FE-SEM images of samples NM-0 (a, e), NM-1/8 (b, f), NM-1/4 (c, g), and NM-1/2 (d, h)

Sample NC-1/2 is obtained after the carbonization of sample NM-1/2 in an argon atmosphere at 800 °C, which possess a hollow spherical superstructure, composed of ordered rod-like secondary structure as shown in Fig. 4(b-c) and Fig. 4(d-e), similar to sample NM-1/2, indicating that the urchin-like morphology is well inherited during the

carbonization process. XRD pattern of sample NC-1/2 displays five strong peaks (Fig. 4(a)), where the peaks at 2θ = 43.7°, 50.9°, and 74.7° are assigned to ferromagnetic $Fe_{0.64}Ni_{0.36}$ (PDF#47-405)[47-48] and the peaks at 2θ = 42.7° and 62.0° corresponds to MgO (PDF#45-0946)[30], respectively. A little shift of the 2θ diffraction peaks of MgO toward low value are noticed, which is attributed to the doping of Fe ions and Ni ions and further verifies in Eq. 2. Only weak $NiFe_2O_4$ (PDF#54-0964) peaks are observed due to most of $NiFe_2O_4$ particles being reduced to $Fe_{0.64}Ni_{0.36}$ during carbonization process[47-48]. The detailed structure of sample NC-1/2 was characterized by HR-TEM and HAADF-STEM and shown in Fig. 4(f), which exhibited limited graphitized carbon (the total carbon content in sample NC-1/2 is 4.6 wt.% according to the weight loss of the sample NC-1/2 after immersing three times with 17% HCl for total 12 h at 80 °C.). Furthermore, the observed lattice spacing of 0.212 nm in Fig. 4(g) (partial enlarged view of Fig. 4(f)) corresponds to the (2 0 0) plane of MgO, which is slightly larger than that of standard MgO[30] due to the doping of Fe and Ni. The extra lattice spacing of 0.204 nm was found in Fig. 4(h) (partial enlarged view of Fig. 4(f)), which is in good agreement with the (1 1 1) plane of $Fe_{0.64}Ni_{0.36}$[47]. Elemental mapping analysis further clarified the uniform distribution of Mg, Fe, Ni, O, and C elements (Fig. 4(i-n)).

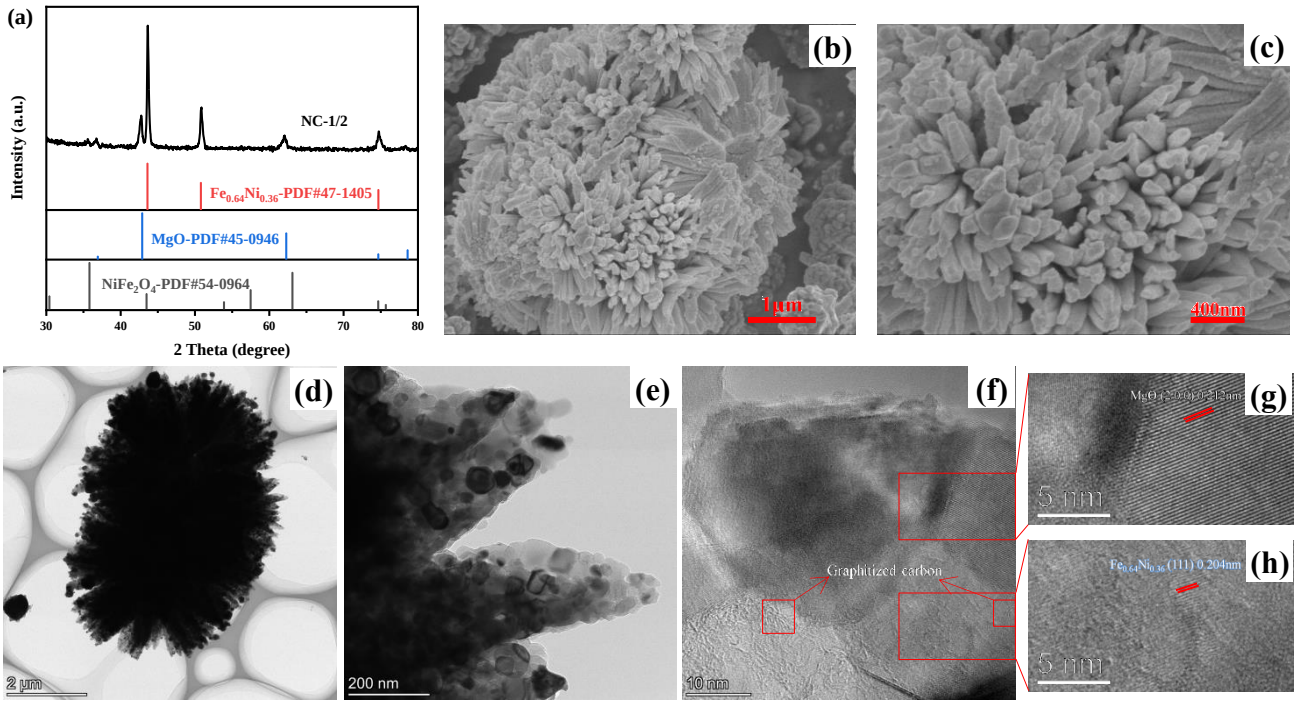

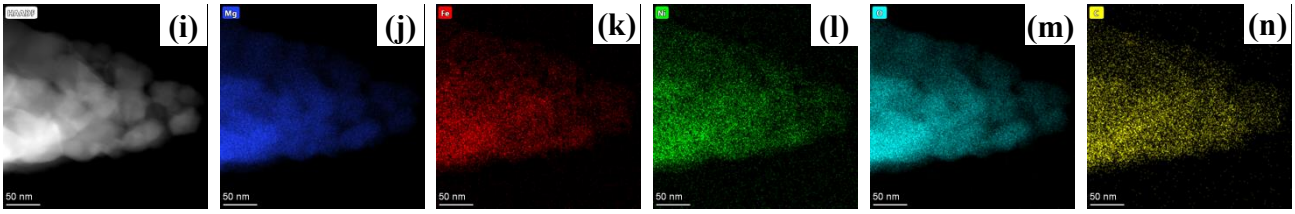

Figure 4 (a) XRD pattern of sample NC-1/2; (b, c) SEM images of sample NC-1/2; (d-h) TEM and HRTEM images of sample NC-1/2; (i) HAADF-STEM images of NC-1/2 and corresponding elemental mapping images of (j) Mg, (k) Fe, (l) Ni, (m) O, and (n) C elements

N_2 adsorption / desorption isotherms and pore size distribution of sample NC-1/2 are analyzed and shown in Fig. 5(a). Sample NC-1/2 owns a low BET surface area of 10.9 m^2 g^{-1} and pore volume of 0.05 cm^3 g^{-1}, mainly contributed by mesopores (inset of Fig. 5(a)), confirming a completely destroyed crystal structure of sample NM-1/2. The generation of mesopores is conducive to charge transfer and mass transportation[49]. Fig. 5(b) shows the Raman spectrum of sample NC-1/2, and two typical D and G peak of carbon located at 1343 cm^{-1} and 1586 cm^{-1} were observed[50]. The value of I_G/I_D in sample NC-1/2 is calculated to be 0.65, suggesting the limited graphitized carbon, which can be noticed in HRTEM (Fig. 4(f)). In addition, the magnetic properties of samples NM-1/2 and NC-1/2 were measured. As shown in Fig. 5(c), sample NC-1/2 achieves much higher saturation magnetization of 57.8 emu g^{-1} than that of sample NM-1/2 (12.2 emu g^{-1}).

Surface chemical compositions of sample NC-1/2 are further studied by XPS analysis. Mg 1s, Fe 2p, Ni 2p, O 1s, and C 1s are all detected (Fig. 5(d)). As shown in Fig. 5(e), the Mg 1s peak can be split into two individual peaks centered at 1301.7 and 1303.1 eV, being attributed to Mg^{2+} in periclase MgO structure and Mg^{2+} in strong interaction with metal atoms in Mg-O-metal bonds (metal = Fe, Ni)[51], respectively, being consistent with XRD results (Fig. 4(a)). The Fe $2p_{3/2}$ spectra of sample NC-1/2 (Fig. 5(f)) show three peaks centered at 705.2, 708.8 and 710.7 eV, corresponding to Fe^0, Fe^{2+}, and Fe^{3+}, respectively, suggesting the surface oxidized Fe species[52]. And Ni $2p_{3/2}$ peak of sample NC-1/2 (Fig. 5(g)) can be split into four individual peaks centred at 850.9, 852.9, 854.3, and 857.2 eV, being attributed to the Ni^0, Ni^{2+} in surface oxidized Ni species, Ni^{2+} in Ni-O-Mg bonds, and Ni^{3+}, respectively[39, 53].

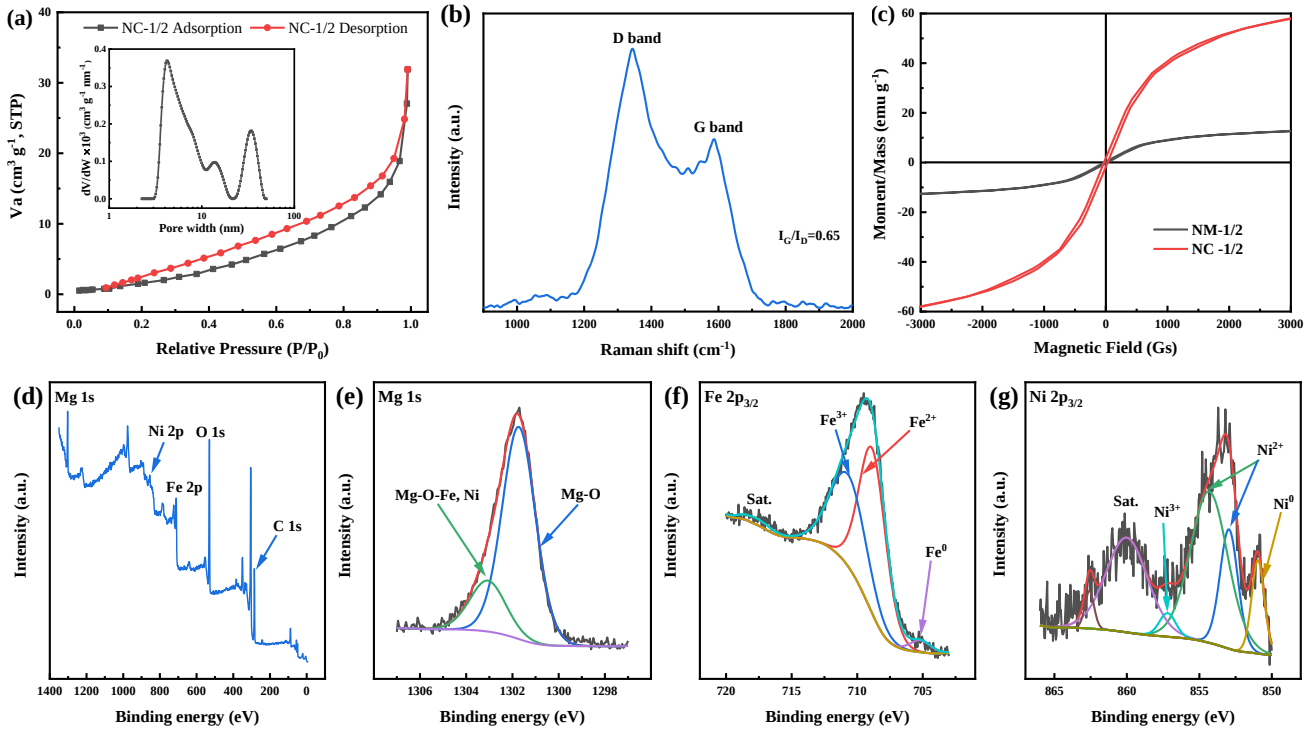

Figure 5 (a) N_2 adsorption / desorption isotherms and pore size distribution curves of sample NC-1/2; (b) Raman spectrum of sample NC-1/2; (c) Hysteresis loops of samples NM-1/2 and NC-1/2 (d) XPS wide spectrum and high resolution spectra of (e) Mg 1s, (f) Fe $2p_{3/2}$, and (g) Ni $2p_{3/2}$ of sample NC-1/2

2.2 Hydrogen Evolution Reaction of the Electrocatalysts

The HER performances of all samples were investigated in 1 M KOH solution. Fig. 6(a) shows the polarization curves of all samples with iR correction. Sample NM-0, pure Mg-MOF-74, shows the worst HER activity with an overpotential (@ 10 mA cm^{-2}) of 696 mV due to the poor conductivity of MOFs, while samples NM-1/8, NM-1/4, and NM-1/2 all owns a smaller overpotential of 671 mV, 649 mV, 615 mV, respectively. Particularly, sample NC-1/2 achieves the smallest overpotential of 403 mV at the current density of 10 mA cm^{-2}. Tafel slopes obtained from LSV curves are shown in Fig. 6(b-c). The Tafel slope of sample NC-1/2 is 106 mV dec^{-1}, much lower than that of samples NM-0 (268 mV dec^{-1}), NM-1/8 (181 mV dec^{-1}), NM-1/4 (147 mV dec^{-1}), and NM-1/2 (141 mV dec^{-1}), suggesting its enhanced HER kinetics[54-55].

The Nyquist curves shown in Fig. 6(d) indicate that sample NC-1/2 displays the smallest semicircle diameter than other samples, demonstrating a faster charge transfer rate[56], but a slightly larger electrolyte resistance, which is

related to the form of MgO with poor electrical conductivity (the content of MgO in the sample is 39.8 wt.%. The calculation details are shown in Supporting Information). Besides, electrochemically active surface areas (ECSA) estimated by C_{dl} is also used to evaluate the HER activity of samples[49]. As shown in Fig. 6(e), sample NC-1/2 exhibits a C_{dl} value of 5.41 mF cm^{-2}, much larger than those of samples NM-0 (1.42 mF cm^{-2}), NM-1/8 (1.29 mF cm^{-2}), NM-1/4 (1.83 mF cm^{-2}), and NM-1/2 (2.84 mF cm^{-2}), supporting its excellent HER activity[28, 49]. The stability of sample NC-1/2 is tested at a current density of 10 mA cm^{-2}, which is shown in Fig. 6(f). It is clear that sample NC-1/2 can keep HER activity for more than 12 h.

Above results shows that NFO@MOF-74 all display a better HER performance than sample NM-0 (the order is NM-1/2 > NM-1/4 > NM-1/8 > NM-0), which comes down to the introduction of NFO NPs leading to improved conductivity, and larger pore volumes of hierarchical superstructures promoting mass transfer[49]. Moreover, sample NC-1/2 provides the best HER activity, which is attributed to the production of graphitized carbon and $Fe_{0.64}Ni_{0.36}$ alloy of improving the electrical conductivity and promote the charge transfer rate[50], and amorphous carbon of providing the additional active sites during the carbonization process[54].

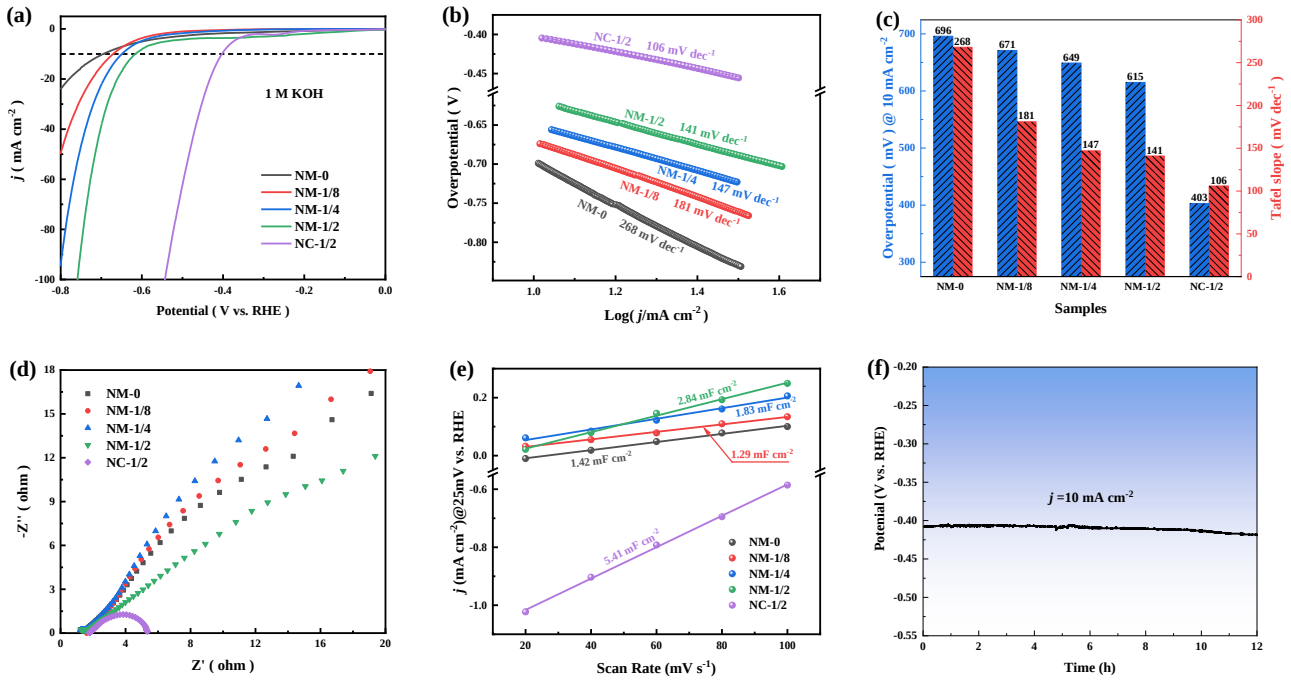

Figure 6 (a) LSV curves with iR correction for HER and (b) corresponding Tafel slopes of all samples in 1 M KOH solution; (c) Summary of overpotential (@ 10 mA cm^{-2}) and Tafel slopes for each sample; (d) Nyquist curves and (e) C_{dl} plots of all samples; (f) Stability test of sample NC-1/2 at 10 mA cm^{-2}

In addition, the HER performance of samples NM-0, NC-1/2 and NFO NPs in a wide range of applied voltage was tested under different ACMF (Supporting Information, Table S1) and shown in Fig. 7(a-b) and Fig. S7 (Supporting Information, Fig. S7). Fig. 7(c) demonstrates that sample NC-1/2 all performs a smaller HER overpotential (@ 10 mA cm^{-2}) in the presence of different ACMF. Especially, sample NC-1/2-5 achieves the smallest overpotential of 372 mV under a much small ACMF of 2.3 mT, which is reduced by 7.7 % compared with no ACMF. Fig. 7(d) reveals the magnetic current density (j_M) of sample NC-1/2 in 1 M KOH solution under different ACMF. It can be found that the reduction peak of metal ions moves to the low voltage region under the ACMF. Interestingly, there exists critical magnetic induction intensity (B_L). The magnetic current density increases with the increase of the magnetic induction intensity (B) when $B < B_L$, and the opposite result is obtained during the HER process while $B > B_L$. That's to say, it is not that the greater the AC magnetic field strength, the higher the HER activity. Moreover, the magnetic current density does not increase monotonously with the increase of applied voltage, but increases first in the voltage range of -0.27 V ~ -0.43 V, and then decreases in a zigzag manner within the voltage range of -0.43 V ~ -0.57 V. Furthermore, sample NM-0 and NFO NPs both showed similar results.

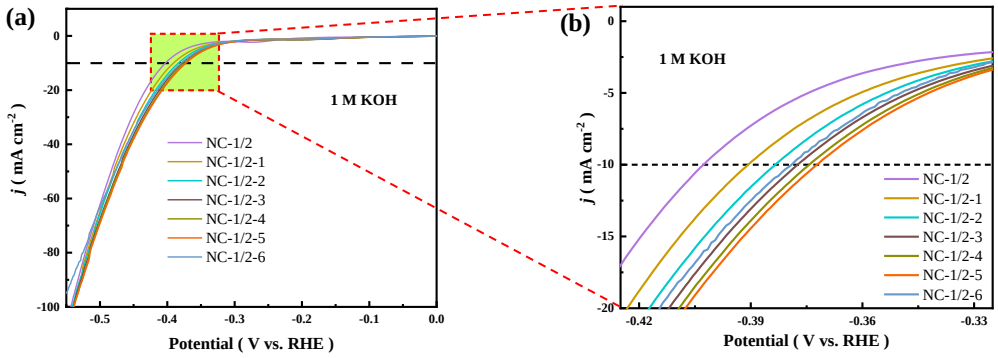

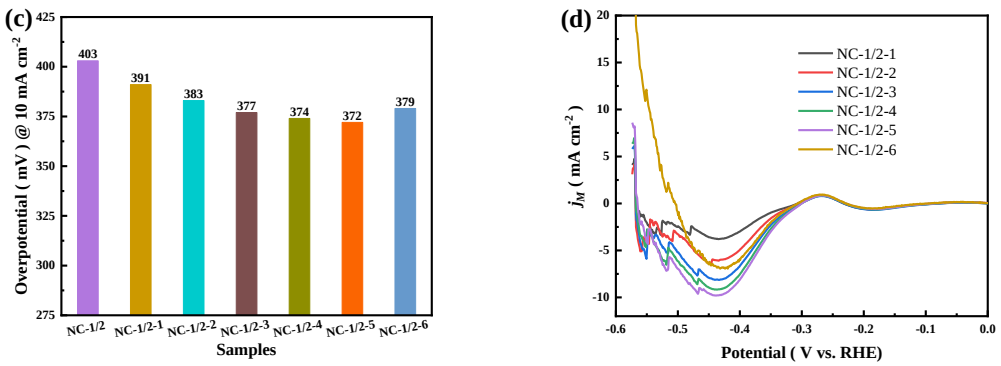

Figure 7 (a-b) LSV curves with iR correction for HER; (c) Histogram of overpotential (@ 10 mA cm^{-2}) and (d) Magnetic current density of sample NC-1/2 in 1 M KOH solution under different ACMF

Here, the unusual HER behavior under an ACMF was studied from a thermodynamic perspective. Scheme 2 showed the schematic diagram of the electrolysis cell and the electrode energization (E_0) after adding ACMF. Firstly, the magnetic catalyst could generate heat under ACMF[17]. Secondly, ACMF could generate an induced electromotive force (E_B) that changes with the magnetic field in electrocatalysts according to Lenz's law. In particular, when a changing current passes through the electrode, an induced electromotive force ($E_{\Delta I}$) in the opposite direction will be generated on the electrode. Finally, the Lorentz force F_L could change the original motion path of the charge / ion under the ACMF and promote the migration of the charge in the electrode phase and the solution phase[14], which is equivalent to adding an extra voltage (E_F) to the electrode. The changing trend of various electromotive forces was described in Fig. 8(a). Also, the ACMF can provide additional energy[57]. Therefore, the total free-energy change consists of three parts under the ACMF: the thermal Gibbs free energy $\Delta G_T(T)$, the electric Gibbs free energy $\Delta G_E(T, E)$, and the magnetic Gibbs free energy $\Delta G_B(T, B)$, as shown in Eq. 3.

$$\Delta G = \Delta G_T + \Delta G_B + \Delta G_E \quad \text{Eq. 3}$$

Here, the magnetic Gibbs free energy is calculated by Eq. 4[57].

$$\Delta G_B = -\frac{1}{2}\mu_0 \chi_V B^2 \quad \text{Eq. 4}$$

Where μ_0 is the vacuum permeability, H / m; χ_v is the volume magnetic susceptibility of the substance; and B is the magnetic induction intensity, T.

And the electric Gibbs free energy can be expressed as:

$$\Delta G_E = -zFE = -zF\left(E_0 + E_B + E_{\Delta I} + E_F\right) \quad \text{Eq. 5}$$

Where z is the number of transferred electrons in the reaction, F is the Faraday constant, E is the electromotive force of the reaction.

As a reaction of increasing entropy, the thermal Gibbs free energy (ΔG_T) decreases as the temperature increases, and a negative magnetic Gibbs free energy (ΔG_B) is obtained when a magnetic field is applied, which also can promote HER[57]. Fig. 8(b) illustrated the change trend of ΔG_T, ΔG_B, ΔG_E, and ΔG. As shown in Fig. 8(b), while $E_0 < E_0$ ($j_{M\,max}$), at this time, ΔG_E ($E_{\Delta I} + E_B + E_F$) < $\Delta G_T + \Delta G_B$, the positive effect of the magnetic field is greater than its negative effect, which manifests as an accelerated HER. When the applied voltage continues to increases ($E_0 > E_0$ ($j_{M\,max}$)), the magnetic current density begins to weaken due to ΔG_E ($E_{\Delta I} + E_B + E_F$) > $\Delta G_T + \Delta G_B$. Especially, ΔG reaches the minimum value at E_0 ($j_M = 0$), the magnetic current density returns to zero, implying that the promotion effect of ACMF on HER is completely eliminated. As the applied voltage increases ($E_0 < E_0$ ($j_M = 0$)) or the magnetic field strengthens ($B > B_L$), an increasing ΔG is gained, which could suppress HER, confirmed by a positive magnetic current density. Therefore, the key to promoting HER is the appropriate magnetic field and the proper applied voltage.

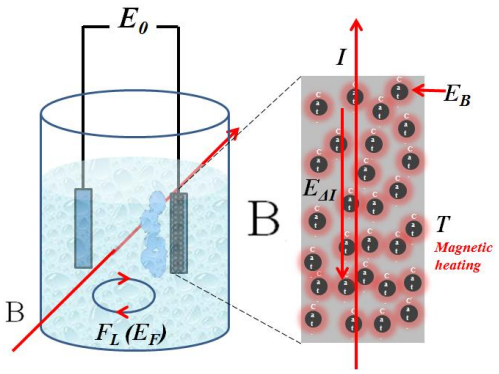

Scheme 2 Diagram of the electrolysis cell and the electrode energization after adding ACMF

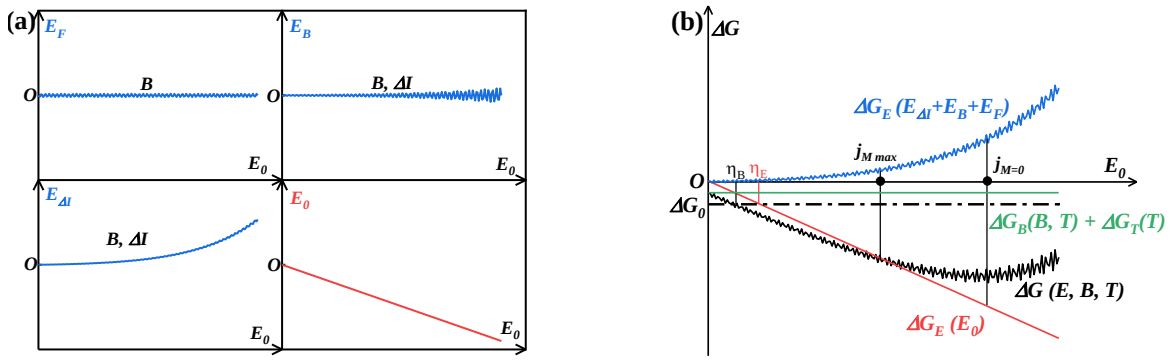

Figure 8 Changing trends schematic diagram of various electromotive forces (a) and Δ*G* (b) under ACMF

3 Conclusions

In summary, a novel strategy was proposed for the synthesis of a magnetic spherical superstructure $NiFe_2O_4$ @ MOF-74 composed of sub-micron rods by dissolving NFO NPs. And a morphology-preserved ferromagnetic superstructure was obtained in the subsequent carbonization process and exhibited a lower overpotential (403 mV @ 10 mA cm^{-2}) than that of $NiFe_2O_4$ @ MOF-74. With the application of an AC magnetic field, the overpotential (@ 10 mA cm^{-2}) for HER decreased first with the increase of the magnetic field strength and then increased. The ferromagnetic superstructure achieves the smallest overpotential (372 mV @ 10 mA cm^{-2}) when an AC magnetic field of 2.3 mT is applied. Besides, a positive effect first appeared, and then weakened, and a negative effect was finally observed as the applied voltage increased, which was attributed to the increasing induced electromotive force and changing Gibbs free energy caused by the applied AC magnetic field. This work helps to more comprehensively understand the effect of external magnetic field on the performance of electrocatalyst for HER, which has wide potential applications in the field of electrocatalysis.

Associated content

Supporting Information Available: Materials and reagents, experimental details, characterization methods, electrochemical measurements, and calculation of magnetic field and the content of the composition of sample NC-1/2; XPS, SEM images, Magnetic current density of related materials.

Acknowledgement

This work is supported by the Natural Science Foundation of Hunan Province (2018JJ4011).

Conflict of interest

There is no interest conflict with others.

References

(1) Wang, J. H.; Cui, W.; Liu, Q.; Xing, Z. C.; Asiri, A. M.; Sun, X. P. Recent Progress in Cobalt-Based Heterogeneous Catalysts for Electrochemical Water Splitting. *Adv. Mater.* **2016,** *28* (2), 215-230.

(2) Zhang, W. X.; Cui, L.; Liu, J. Q. Recent Advances in Cobalt-based Electrocatalysts for Hydrogen and Oxygen Evolution Reactions. *J. Alloys Compd.* **2020,** *821*, 153542.

(3) Chu, W. J.; Shi, Z. J.; Hou, Y. D.; Ma, D. N.; Bai, X.; Gao, Y. F.; Yang, N. J. Trifunctional of Phosphorus-Doped $NiCo_2O_4$ Nanowire Materials for Asymmetric Supercapacitor, Oxygen Evolution Reaction, and Hydrogen Evolution Reaction. *ACS Appl. Mater. Interfaces* **2020,** *12* (2), 2763-2772.

(4) Lu, J.; Ji, S.; Kannan, P.; Wang, H.; Wang, X.; Wang, R. Hydrophilic $Ni(OH)_2$@CoB Nano-chains with Shell-Core Structure as an Efficient Catalyst for Oxygen Evolution Reaction. *J. Alloys Compd.* **2020,** *844*, 156129.

(5) Yu, F.; Zhou, H. Q.; Huang, Y. F.; Sun, J. Y.; Qin, F.; Bao, J. M.; Goddardiii, W. A.; Chen, S.; Ren, Z. F. High-performance Bifunctional Porous non-noble Metal Phosphide Catalyst for Overall Water Splitting. *Nat. Commun.* **2018**, *9*, 2551.

(6) Shi, Q.; Zhu, C.; Du, D.; Lin, Y. Robust Noble Metal-based Electrocatalysts for Oxygen Evolution Reaction. *Chem. Soc. Rev.* **2019,** *48* (12), 3181-3192.

(7) Wang, Z. N.; Wang, H.; Ji, S.; Wang, X. Y.; Pollet, B. G.; Wang, R. F. Multidimensional Regulation of Ni_3S_2 @ $Co(OH)_2$ Catalyst with High Performance for Wind Energy Electrolytic Water. *J. Power Sources* **2020,** *446,* 227348.

(8) Zhang, Y.; Wang, X. X.; Luo, F. Q.; Tan, Y.; Zeng, L. X.; Fang, B. Z.; Liu, A. H. Rock Salt Type $NiCo_2O_3$ Supported on Ordered Mesoporous Carbon as a Highly Efficient Electrocatalyst for Oxygen Evolution Reaction. *Appl. Catal. B Environ.* **2019,** *256*, 117852.

(9) Bund, A.; Koehler, S.; Kuehnlein, H. H.; Plieth, W. Magnetic Field Effects in Electrochemical Reactions. *Electrochim. Acta* **2003,** *49* (1), 147-152.

(10) Zhu, J.; Chen, M.; Qu, H.; Luo, Z.; Wu, S.; Colorado, H. A.; Wei, S.; Guo, Z. Magnetic Field Induced Capacitance Enhancement in Graphene and Magnetic Graphene Nanocomposites. *Energy Environ. Sci.* **2013,** *6* (1), 194-204.

(11) Tatsuhiro Okada, N. I. W., Liangbi Wang , Hiroshi Shingu ,Jun-ich Okano, Takeo Ozawa. The Effect of Magnetic Field on the Oxygen Reduction Reaction and Its Application in Polymer Electrolyte Fuel Cells. *Electrochim. Acta* **2003,** *48*(5), 531-539.

(12) Koza, J. A.; Uhlemann, M.; Gebert, A.; Schultz, L. Desorption of Hydrogen From the Electrode Surface under Influence of an External Magnetic Field. *Electrochem. Commun.* **2008,** *10* (9), 1330-1333.

(13) Koza, J. A.; Mühlenhoff, S.; Uhlemann, M.; Eckert, K.; Gebert, A.; Schultz, L. Desorption of Hydrogen

from an Electrode Surface under Influence of an External Magnetic Field – In-situ Microscopic Observations. *Electrochem. Commun.* **2009,** *11* (2), 425-429.

(14) Li, Y.; Zhang, L.; Peng, J.; Zhang, W.; Peng, K. Magnetic Field Enhancing Electrocatalysis of Co_3O_4 / NF for Oxygen Evolution Reaction. *J. Power Sources* **2019,** *433*, 226704.

(15) Elias, L.; Chitharanjan Hegde, A. Effect of Magnetic Field on HER of Water Electrolysis on Ni–W Alloy. *Electrocatalysis* **2017,** *8* (4), 375-382.

(16) Lin, M.-Y.; Hourng, L.-W.; Kuo, C.-W. The Effect of Magnetic Force on Hydrogen Production Efficiency in Water Electrolysis. *Int. J. Hydrogen Energy* **2012,** *37* (2), 1311-1320.

(17) Niether, C.; Faure, S.; Bordet, A.; Deseure, J.; Chatenet, M.; Carrey, J.; Chaudret, B.; Rouet, A. Improved Water Electrolysis Using Magnetic Heating of FeC–Ni core–shell Nanoparticles. *Nat. Energy* **2018,** *3* (6), 476-483.

(18) Wan, S.; Qi, J.; Zhang, W.; Wang, W.; Zhang, S.; Liu, K.; Zheng, H.; Sun, J.; Wang, S.; Cao, R. Hierarchical Co(OH)F Superstructure Built by Low-Dimensional Substructures for Electrocatalytic Water Oxidation. *Adv. Mater.* **2017,** *29* (28), 1700286.

(19) Sun, L.; Wang, C.; Wang, L. A Kind of Coordination Complex Cement for the Self-Assembly of Superstructure. *ACS Nano* 2018, *12* (4), 4002-4009.

(20) Yao, J.; Wang, W.; Zuo, X.; Yang, Q.; Khan, M. W.; Wu, M.; Tang, H.; Jin, S.; Li, G. Multi-Interface Superstructure Strategy to Improve the Catalytic Activity and Cyclic Stability in Enhancing the Photo Conversion in Solar Cells. *Appl. Catal. B Environ.* **2019,** *256*, 117857.

(21) Guo, J.; Tardy, B. L.; Christofferson, A. J.; Dai, Y.; Richardson, J. J.; Zhu, W.; Hu, M.; Ju, Y.; Cui, J.; Dagastine, R. R.; Yarovsky, I.; Caruso, F. Modular Assembly of Superstructures from Polyphenol-Functionalized Building Blocks. *Nat. Nanotech.* **2016,** *11* (12), 1105-1111.

(22) Zou, L.; Kitta, M.; Hong, J.; Suenaga, K.; Tsumori, N.; Liu, Z.; Xu, Q. Fabrication of a Spherical Superstructure of Carbon Nanorods. *Adv. Mater.* **2019,** *31* (24), 1900440.

(23) Pi, Y.; Zhang, N.; Guo, S.; Guo, J.; Huang, X. Ultrathin Laminar Ir Superstructure as Highly Efficient Oxygen Evolution Electrocatalyst in Broad pH Range. *Nano Lett.* **2016,** *16* (7), 4424-4430.

(24) Furukawa, S.; Reboul, J.; Diring, S.; Sumida, K.; Kitagawa, S. Structuring of Metal-Organic Frameworks at the Mesoscopic/Macroscopic Scale. *Chem. Soc. Rev.* **2014,** *43* (16), 5700-5734.

(25) Bian, Z.; Tachikawa, T.; Zhang, P.; Fujitsuka, M.; Majima, T. Au / TiO_2 Superstructure-based Plasmonic Photocatalysts Exhibiting Efficient Charge Separation and Unprecedented Activity. *J. Am. Chem. Soc.* **2014,** *136* (1), 458-465.

(26) Wu, X. J.; Chen, J.; Tan, C.; Zhu, Y.; Han, Y.; Zhang, H. Controlled Growth of High-Density CdS and CdSe Nanorod Arrays on Selective Facets of Two-Dimensional Semiconductor Nanoplates. *Nat. Chem.* **2016,** *8* (5), 470-475.

(27) Zhong, Y. R.; Lin, F.; Wang, M. Y.; Zhang, Y. F.; Ma, Q.; Lin, J. L.; Feng, Z. X.; Wang, H. L. Metal Organic Framework Derivative Improving Lithium Metal Anode Cycling. *Adv. Funct. Mater.* **2020,** *30* (10), 1907579.

(28) Liu, T.; Li, P.; Yao, N.; Cheng, G. Z.; Chen, S. L.; Luo, W.; Yin, Y. D. CoP-Doped MOF-Based Electrocatalyst for pH-Universal Hydrogen Evolution Reaction. *Angew. Chem. Int. Ed.* **2019,** *58* (14), 4679-4684.

(29) Zeng, L. X.; Fang, Y. X.; Xu, L. H.; Zheng, C.; Yang, M. Q.; He, J. F.; Xue, H.; Qian, Q. R.; Wei, M. D.; Chen, Q. H. Rational Design of Few-layer $MoSe_2$ Confined within ZnSe-C Hollow Porous Spheres for High-Performance Lithium-ion and Sodium-ion Batteries. *Nanoscale* **2019,** *11* (14), 6766-6775.

(30) Lv, Z. M.; Wang, H. Y.; Chen, C. L.; Yang, S. M.; Chen, L.; Alsaedi, A.; Hayat, T. Enhanced Removal of Uranium(VI) from Aqueous Solution by a Novel Mg-MOF-74-Derived Porous MgO / carbon Adsorbent. *J. Colloid Interf. Sci.* **2019,** *537*, A1-A10.

(31) Wang, Y.; Gao, X.; Wu, X. M.; Zhang, W. Z.; Luo, C. Y.; Liu, P. B. Facile Design of 3D Hierarchical $NiFe_2O_4$ / N-GN / ZnO Composite as a High Performance Electromagnetic Wave Absorber. *Chem. Eng. J.* **2019,** *375*, 121942.

(32) Luz, I.; Loiudice, A.; Sun, D. T.; Queen, W. L.; Buonsanti, R. Understanding the Formation Mechanism of Metal Nanocrystal @ MOF-74 Hybrids. *Chem. Mater.* **2016,** *28* (11), 3839-3849.

(33) Xu, T. T.; Hou, X. D.; Liu, S. J.; Liu, B. One-step Synthesis of Magnetic and Porous Ni @ MOF-74(Ni) Composite. *Micropor. Mesopor. Mat.* **2018,** *259*, 178-183.

(34) Chen, J. Y.; Zhuang, P. Y.; Ge, Y. C.; Chu, H.; Yao, L. Y.; Cao, Y. D.; Wang, Z. Y.; Chee, M. O. L.; Dong, P.; Shen, J. F.; Ye, M. X.; Ajayan, P. M. Sublimation-Vapor Phase Pseudomorphic Transformation of Template-Directed MOFs for Efficient Oxygen Evolution Reaction. *Adv. Funct. Mater.* **2019,** *29* (37), 1903875.

(35) Zhang, L.; Li, Y. Y.; Peng, J. H.; Peng, K. Bifunctional $NiCo_2O_4$ Porous Nanotubes Electrocatalyst for Overall Water-Splitting. *Electrochim. Acta* **2019,** *318*, 762-769.

(36) Dong, C. Q.; Kou, T. Y.; Gao, H.; Peng, Z. Q.; Zhang, Z. H. Eutectic-Derived Mesoporous Ni-Fe-O Nanowire Network Catalyzing Oxygen Evolution and Overall Water Splitting. *Adv. Energy Mater.* **2018,** *8* (5), 1701347.

(37) Park, G. D.; Cho, J. S.; Kang, Y. C. Multiphase and Double-Layer $NiFe_2O_4$ @ NiO-Flollow-Nanosphere Decorated Reduced Graphene Oxide Composite Powders Prepared by Spray Pyrolysis Applying Nanoscale Kirkendall Diffusion. *ACS Appl. Mater. Interfaces* **2015,** *7* (30), 16842-16849.

(38) Sun, H.; Ren, D. N.; Kong, R. Q.; Wang, D.; Jiang, H.; Tan, J. L.; Wu, D.; Chen, S. W.; Shen, B. X. Tuning 1-hexene / n-hexane Adsorption on MOF-74 via Constructing Co-Mg Bimetallic Frameworks. *Micropor. Mesopor. Mat.* **2019,** *284*, 151-160.

(39) Man, P.; He, B.; Zhang, Q. C.; Zhou, Z. Y.; Li, C. W.; Li, Q. L.; Wei, L.; Yao, Y. G. A One-Dimensional Channel Self-Standing MOF Cathode for Ultrahigh-Energy-Density Flexible Ni-Zn Batteries. *J. Mater. Chem. A* **2019,** *7* (48), 27217-27224.

(40) Qiu, W. J.; Dou, K.; Zhou, Y.; Huang, H. F.; Chen, Y. F.; Lu, H. F. Hierarchical Pore Structure of Activated Carbon Fabricated by CO_2 / Microwave for Volatile Organic Compounds Adsorption. *Chinese J. Chem. Eng.* 2018, *26* (1), 81-88.

(41) Zhou, L.; Zhuang, Z. C.; Zhao, H. H.; Lin, M. T.; Zhao, D. Y.; Mai, L. Q. Intricate Hollow Structures: Controlled Synthesis and Applications in Energy Storage and Conversion. *Adv. Mater.* **2017,** *29* (20), 1602914.

(42) Ji, D. X.; Fan, L.; Tao, L.; Sun, Y. J.; Li, M. G.; Yang, G. R.; Tran, T. Q.; Ramakrishna, S.; Guo, S. J. The Kirkendall Effect for Engineering Oxygen Vacancy of Hollow Co_3O_4 Nanoparticles toward High-Performance Portable Zinc-Air Batteries. *Angew. Chem. Int. Ed.* **2019,** *58* (39), 13840-13844.

(43) Huo, J.; Wang, L.; Irran, E.; Yu, H. J.; Gao, J. M.; Fan, D. S.; Li, B.; Wang, J. J.; Ding, W. B.; Amin, A. M.; Li, C.; Ma, L. A. Hollow Ferrocenyl Coordination Polymer Microspheres with Micropores in Shells Prepared by Ostwald Ripening. *Angew. Chem. Int. Ed.* **2010,** *49* (48), 9237-9241.

(44) Xie, J. F.; Zhang, X. D.; Zhang, H.; Zhang, J. J.; Li, S.; Wang, R. X.; Pan, B. C.; Xie, Y. Intralayered Ostwald Ripening to Ultrathin Nanomesh Catalyst with Robust Oxygen-Evolving Performance. *Adv. Mater.* **2017,** *29* (10), 1604765.

(45) Yan, L. T.; Cao, L.; Dai, P. C.; Gu, X.; Liu, D. D.; Li, L. J.; Wang, Y.; Zhao, X. B. Metal-Organic Frameworks Derived Nanotube of Nickel-Cobalt Bimetal Phosphides as Highly Efficient Electrocatalysts for Overall Water Splitting. *Adv. Funct. Mater.* **2017,** *27* (40), 1703455.

(46) Feng, L.; Li, J. L.; Day, G. S.; Lv, X. L.; Zhou, H. C. Temperature-Controlled Evolution of Nanoporous MOF Crystallites into Hierarchically Porous Superstructures. *Chem.* **2019,** *5* (5), 1265-1274.

(47) Zhang, C. G.; Li, J. J.; Shi, C. S.; Liu, E. Z.; Du, X. W.; Feng, W.; Zhao, N. Q. The Efficient Synthesis of Carbon Nano-Onions Using Chemical Vapor Deposition on an Unsupported Ni-Fe Alloy Catalyst. *Carbon* **2011,** *49* (4), 1151-1158.

(48) Yan, X.; Xue, D. S. Fabrication and Microwave Absorption Properties of $Fe_{0.64}Ni_{0.36}$-$NiFe_2O_4$ Nanocomposite. *Nano-Micro Lett.* **2012,** *4* (3), 176-179.

(49) Pan, Y.; Sun, K. A.; Liu, S. J.; Cao, X.; Wu, K. L.; Cheong, W. C.; Chen, Z.; Wang, Y.; Li, Y.; Liu, Y. Q.; Wang, D. S.; Peng, Q.; Chen, C.; Li, Y. D. Core-Shell ZIF-8 @ ZIF-67-Derived CoP Nanoparticle-Embedded N-Doped Carbon Nanotube Hollow Polyhedron for Efficient Overall Water Splitting. *J. Am. Chem. Soc.* **2018,** *140* (7), 2610-2618.

(50) Lu, X. F.; Gu, L. F.; Wang, J. W.; Wu, J. X.; Liao, P. Q.; Li, G. R. Bimetal-Organic Framework Derived $CoFe_2O_4$ / C Porous Hybrid Nanorod Arrays as High-Performance Electrocatalysts for Oxygen Evolution Reaction. *Adv. Mater.* **2017,** *29* (3), 1604437

(51) Uhl, F.; Staemmler, V. An ab Initio Study of the O1s and Mg1s, Mg2s, Mg2p Core Electron Binding Energies in Bulk MgO. *J. Electron Spectrosc. Relat. Phenom.* **2019,** *233*, 90-96.

(52) Hu, Q.; Liu, X. F.; Tang, C. Y.; Fan, L. D.; Chai, X. Y.; Zhang, Q. L.; Liu, J. H.; He, C. X. Facile Fabrication of a 3D Network Composed of N-doped Carbon-Coated Core-Shell Metal Oxides / Phosphides for Highly Efficient Water Splitting. *Sustain. Energ. Fuels* **2018,** *2* (5), 1085-1092.

(53) Hu, Q.; Liu, X. F.; Zhu, B.; Fan, L. D.; Chai, X. Y.; Zhang, Q. L.; Liu, J. H.; He, C. X.; Lin, Z. Q. Crafting MoC_2-Doped Bimetallic Alloy Nanoparticles Encapsulated within N-doped Graphene as Roust Bifunctional Electrocatalysts for Overall Water Splitting. *Nano Energy* **2018,** *50*, 212-219.

(54) Zhou, Q. Q.; Wang, J. Y.; Guo, F. Y.; Li, H. W.; Zhou, M. Z.; Qian, J. J.; Li, T. T.; Zheng, Y. Q. Self-Supported Bimetallic Phosphide-Carbon Nanostructures Derived from Metal-Organic Frameworks as Bifunctional Catalysts for Highly Efficient Water Splitting. *Electrochim. Acta* **2019,** *318*, 244-251.

(55) Wang, X. X.; Liu, R. P.; Zhang, Y.; Zeng, L. X.; Liu, A. H. Hierarchical Ni_3S_2-NiOOH Hetero-Nanocomposite Grown on Nickel Foam as a Noble-Metal-Free Electrocatalyst for Hydrogen Evolution Reaction in Alkaline Electrolyte. *Appl. Surf. Sci.* **2018,** *456*, 164-173.

(56) Wang, Z. N.; Ji, S.; Liu, F. S.; Wang, H.; Wang, X. Y.; Wang, Q. Z.; Pollet, B. G.; Wang, R. F. Highly Efficient and Stable Catalyst Based on $Co(OH)_2$ @ Ni Electroplated on Cu-Metallized Cotton Textile for Water Splitting. *ACS Appl. Mater. Interfaces* **2019,** *11* (33), 29791-29798.

(57) Wang, J. H.; Ma, Y. W.; Watanabe, K. Magnetic-Field-Induced Synthesis of Magnetic Gamma-Fe_2O_3 Nanotubes. *Chem. Mater.* **2008,** *20* (1), 20-22.

Table of Contents Graphic